CELL BIOLOGY

Compression-induced dedifferentiation of adipocytes promotes tumor progression

Yiwei Li[1], Angelo S. Mao[2,3], Bo Ri Seo[2,3], Xing Zhao[1], Satish Kumar Gupta[1], Maorong Chen[4], Yu Long Han[1], Ting-Yu Shih[2,3], David J. Mooney[2,3], Ming Guo[1]*

Dysregulated physical stresses are generated during tumorigenesis that affect the surrounding compliant tissues including adipocytes. However, the effect of physical stressors on the behavior of adipocytes and their cross-talk with tumor cells remain elusive. Here, we demonstrate that compression of cells, resulting from various types of physical stresses, can induce dedifferentiation of adipocytes via mechanically activating Wnt/β-catenin signaling. The compression-induced dedifferentiated adipocytes (CiDAs) have a distinct transcriptome profile, long-term self-renewal, and serial clonogenicity, but do not form teratomas. We then show that CiDAs notably enhance human mammary adenocarcinoma proliferation both in vitro and in a xenograft model, owing to myofibrogenesis of CiDAs in the tumor-conditioned environment. Collectively, our results highlight unique physical interplay in the tumor ecosystem; tumor-induced physical stresses stimulate de novo generation of CiDAs, which feedback to tumor growth.

INTRODUCTION

Tumor progression and metastasis not only are driven by the state of the cancer cells independently but also are notably affected by its interactions with the complex heterogeneous ecosystem surrounding it, commonly known as the tumor stroma (*1*, *2*). This microenvironment comprises the extracellular matrix (ECM), basement membrane, fibroblasts, adipocytes, endothelial cells, and immune cells, all of which regulate the behavior and coevolve with cancer cells throughout various stages of cancer progression (*2*–*4*). Among them, adipocytes constitute a major component of the breast stroma and have garnered attention owing to the significant emerging evidence demonstrating a reciprocal metabolic adaptation between them and the breast cancer cells (*5*, *6*). Moreover, previous studies have also demonstrated that obesity with increasing worldwide prevalence has been a major risk for several types of cancer by means of inducing adipose tissue dysfunction (*7*, *8*). They attribute this correlation to a biochemical interplay where adipocytes interact with cancer cells through paracrine signals that are released locally within the tumor microenvironment as well as the endocrine signals that originate from distal adipose tissue that may significantly disrupt local metabolic homeostasis (*5*, *9*, *10*). Nevertheless, these interesting studies mostly focus on the biochemical pathways of the interactions between cancer cells and adipocytes and do not incorporate the physical changes experienced by the tumor stroma. However, numerous recent evidence suggests that rapid expansion of solid tumors can significantly alter the local physical microenvironment by compressing the surrounding stroma (*11*, *12*), stiffening the matrix (*12*, *13*), and increasing the osmotic pressure in surrounding tissues (*14*–*16*). These changes result in dysregulated physical stresses that may play an important role in tumor progression via altering signaling (*11*, *17*), remodeling surrounding ECM (*13*, *17*), and mediating epithelial-to-mesenchymal transition (*18*–*20*). Adipocytes in the tumor microenvironment are subject to these changes, experiencing, for instance, 10 times greater matrix stiffness (*21*), significantly increased solid stresses (*12*), and more than two times greater osmotic pressure (*16*). Previous studies have shown that multipotent adipose-derived stem cells used for soft tissue reconstruction following mastectomy undergo myofibroblastic differentiation due to soluble factors from breast cancer cells and correlate it to varied ECM deposition and contraction, thereby enhancing tissue stiffness (*21*–*24*). However, the impact of dysregulated physical stresses in the tumor microenvironment on associated adipocytes is not well understood. Moreover, the cross-talk between the physical and biochemical/metabolic interactions remains elusive.

Here, we find the effect of physical stresses on adipocytes and assess whether these changes feedback to the progression of mammary tumor cells and together alter the evolution of the tumor ecosystem. Our results demonstrate that compression of adipocytes resulting from various types of physical stresses can induce their dedifferentiation via mechanically activating Wnt/β-catenin signaling. The compression-induced dedifferentiated adipocytes (CiDAs) have a distinct transcriptome profile, long-term self-renewal, and serial clonogenicity (including osteogenesis, adipogenesis, myogenesis, chondrogenesis, and myofibrogenesis) but do not form teratomas. We believe that the adipocytes dedifferentiate into a state that is similar to mesenchymal stem cells (MSCs) but do not go further back to a more naïve state and, thus, do not form teratomas. This is consistent with previous studies that have shown that reprogrammed stem cells that are more naïve than MSCs can form teratoma (*25*, *26*). Subsequently, we show that CiDAs significantly enhance human mammary adenocarcinoma MDA-MB-231 cell proliferation both in vitro and in a xenograft model. We identify myofibrogenesis of CiDAs in the tumor-conditioned environment, which, in turn, contributes to the enhanced tumor growth. Collectively, our results suggest that tumor-induced physical stresses stimulate de novo generation of CiDAs by physically reprogramming surrounding adipocytes, which could differentiate into myofibroblasts in the tumor microenvironment and then feedback to the tumor cells to enhance their growth.

[1]Department of Mechanical Engineering, Massachusetts Institute of Technology, Cambridge, MA 02139, USA. [2]John A. Paulson School of Engineering and Applied Sciences, Harvard University, Cambridge, MA 02138, USA. [3]Wyss Institute for Biologically Inspired Engineering, Harvard University, Cambridge, MA 02138, USA. [4]F. M. Kirby Neurobiology Center, Boston Children's Hospital, Department of Neurology, Harvard Medical School, Boston, MA 02115, USA.
*Corresponding author. Email: guom@mit.edu

RESULTS

Physical compression induces dedifferentiation of adipocytes

To first study the impact of increased osmotic pressure on adipocytes either generated from a mouse MSC line, OP9s, or primary human preadipocytes, we culture them in a hypertonic medium (Fig. 1A) to mimic the elevated osmotic pressure in the tumor microenvironment. We find that almost half of the adipocytes lose visible lipid droplets under a hypertonic pressure of 400 mosmol, which simulates the elevated pressure in the tumor (Fig. 1, B to D). The remaining adipocytes also experience a decrease in lipid droplet size and, furthermore, adopt a spindle-like shape with an aspect ratio of 5.8 ± 0.6. In comparison, 90% of adipocytes cultured under isotonic condition retain lipid droplets and maintain a more spherical morphology, with an aspect ratio of 2.8 ± 0.5 (Fig. 1E). To evaluate the ability of adipocyte postexposure to hypertonic medium to undergo multipotent differentiation, further experiments confirm that these cells are capable of undergoing osteogenesis (Fig. 1, F and G, and fig. S1, A and B), myogenesis (Fig. 1, H and I), and adipogenesis (Fig. 1, J and K) via culture under respective differentiation induction media (see the Supplementary Materials). The adipocytes under hypertonic medium gradually spread, elongate, and lose intracellular lipid droplets (Fig. 2A). Moreover, exposure to hypertonic medium enables the adipocytes to adopt a branched morphology (Fig. 2, B and C), divide (Fig. 2D), and undergo migration (Fig. 2, E and F), qualities characteristic of MSCs but distinct from adipocytes. To rule out the possibility that hypertonicity is selecting for a preexisting population of less differentiated adipocytes, we analyze the compression-induced dedifferentiation of individual adipocytes and their subsequent characteristics. Human adipocytes are sorted from nondifferentiated cells via density separation, individual adipocytes are cultured singly in separate wells, so as to preclude possible paracrine effects when cells are growing in population, and their behavior under hypertonic and isotonic media is tracked (Fig. 3, A and B). Similar to population-level findings, 36.5 ± 8.9% and 49.3 ± 3.7% of adipocytes lose visible fat droplets (see the Supplementary Materials) when cultured in hypertonic medium of 363 and 400 mosmol, respectively (Fig. 3C).

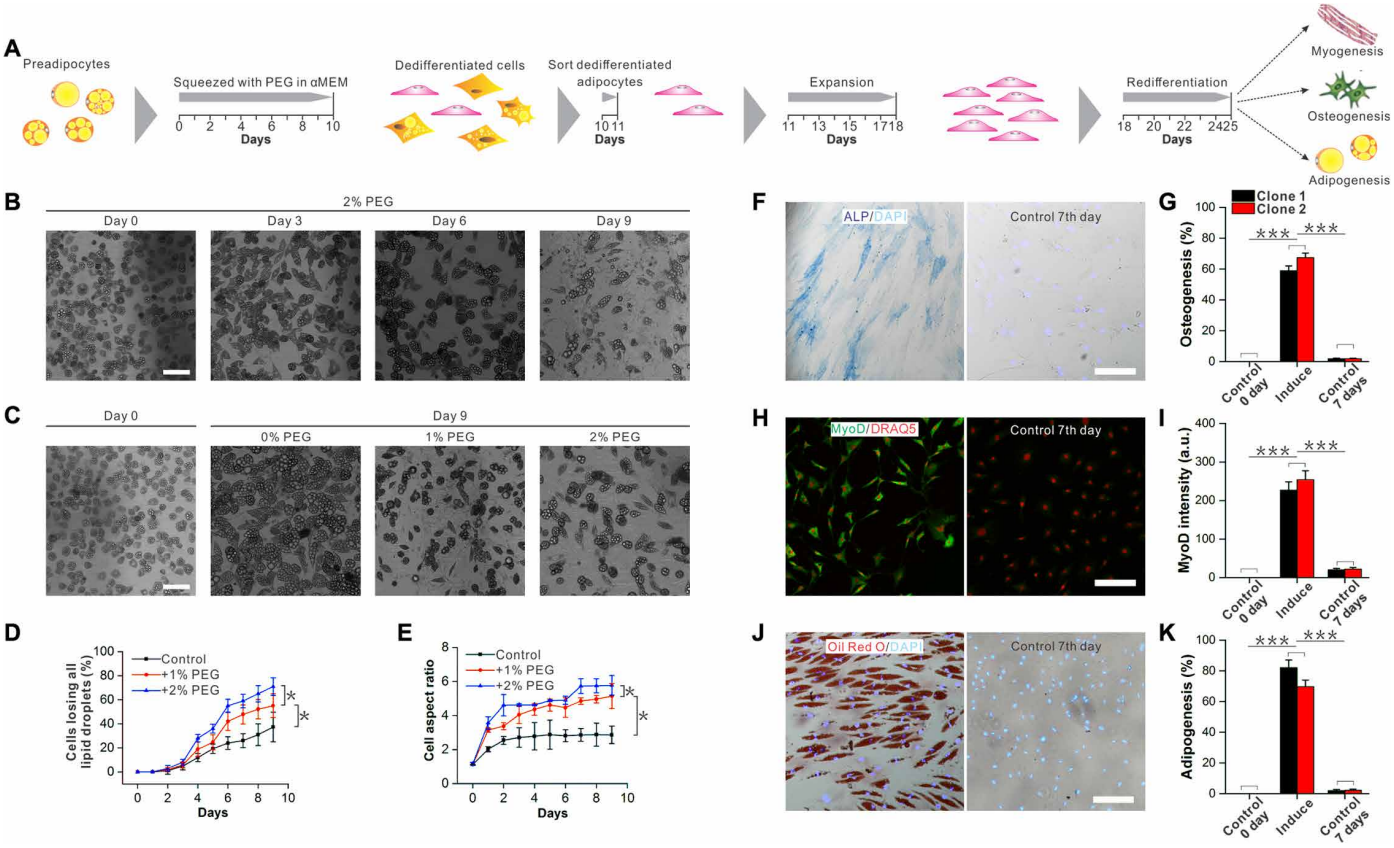

Fig. 1. Compression-induced dedifferentiation of adipocytes. (**A**) Schematic outline of the compression treatment schedule. The adipocytes are compressed in hypertonic medium for 10 days and then incubated in expansion medium for another 2 weeks. The colonies of expanded dedifferentiated adipocytes are further redifferentiated into myoblasts, osteocytes, and adipocytes. (**B**) Images showing that the number of adipocytes decreases over time under osmotic compression. Scale bar, 100 μm. (**C**) Images showing the decreased number of adipocytes as we increase osmotic pressure. Scale bar, 100 μm. (**D**) Quantification of adipocytes losing all their obvious lipid droplets during 10 days of culture. Osmotic compression significantly increases the ratio of adipocytes that lose all their obvious lipid droplets. Error bars represent SD ($n = 3$). (**E**) Measurements of the diameter of intracellular lipid droplets of adipocytes. Osmotic compression slightly decreases the size of lipid droplets. The size of intracellular lipid droplets keeps increasing when adipocytes are cultured without osmotic compression. Error bars represent SD ($n = 3$). (**F** and **G**) Images (F) and quantification (G) of alkaline phosphatase (ALP) showing osteogenic potential of CiDAs. Scale bar, 50 μm. Error bars represent SD ($n = 3$). DAPI, 4′,6-diamidino-2-phenylindole. (**H** and **I**) Images (H) and quantification (I) of MyoD showing the myogenic potential of CiDAs. Scale bar, 50 μm. Error bars represent SD ($n = 3$). a.u., arbitrary units. (**J** and **K**) Images (J) and quantification (K) of Oil Red O showing the adipogenic potential of CiDAs. Scale bar, 50 μm. Error bars represent SD ($n = 3$). *$P < 0.05$ and ***$P < 0.001$.

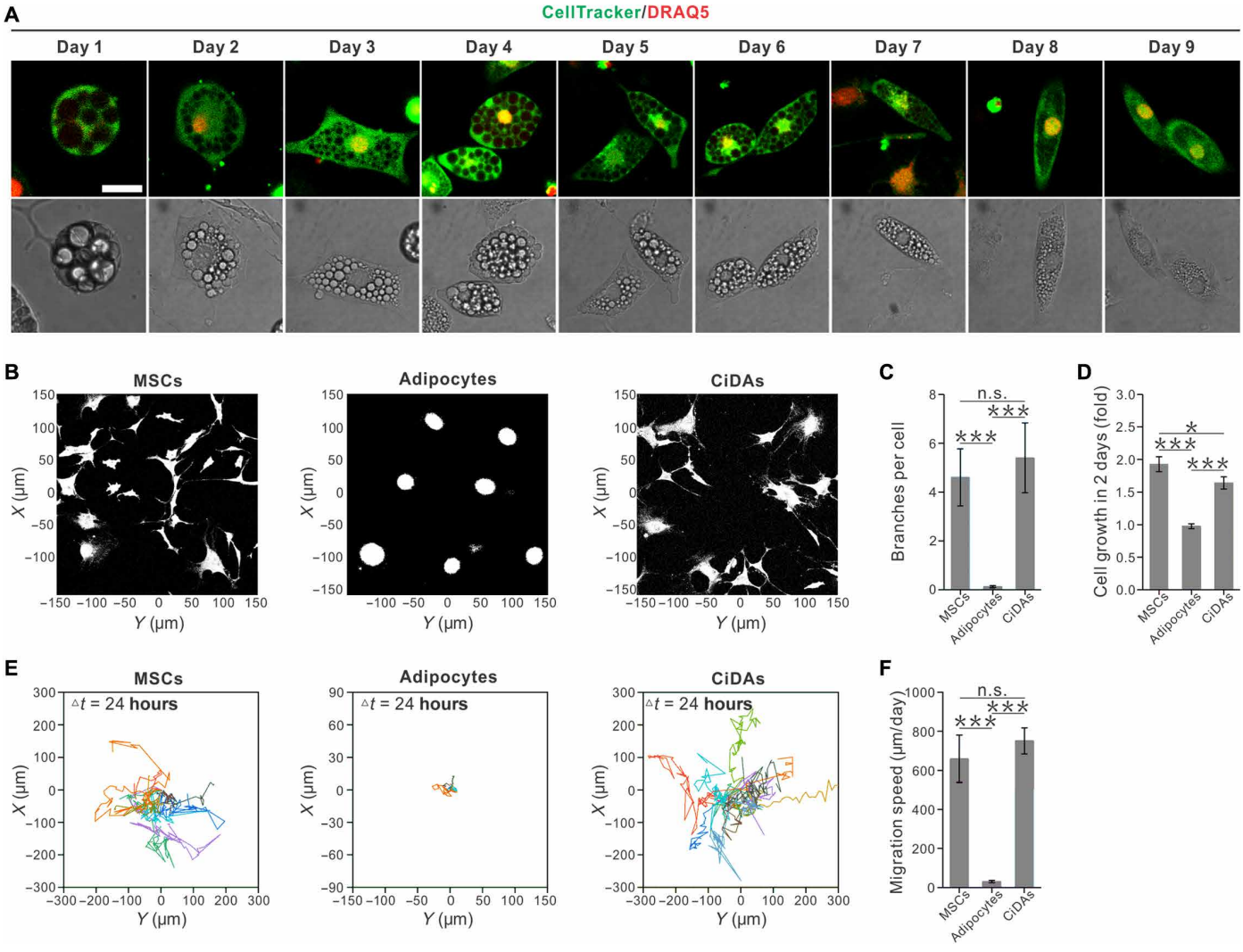

Fig. 2. Biophysical characterization of adipocytes under dedifferentiation induced by compression. (**A**) Fluorescence images (top) and bright-field images (bottom) showing that the adipocytes gradually lose their lipid droplets, spread, and elongate under osmotic compression. Green indicates the cytoplasm, while red indicates the nucleus. Scale bar, 20 μm. (**B**) Images showing significant difference in the cellular morphologies of MSCs, adipocytes, and CiDAs. (**C**) Quantification of branches per cell showing that both MSCs and CiDAs have similar numbers of branches, while the adipocytes exhibit a round morphology. n.s., not significant. (**D**) Measurements showing that CiDAs regain the ability to proliferate similar to MSCs. (**E** and **F**) Cell migration trajectory and corresponding migration rates. CiDAs regain the ability to migrate similar to MSCs, while no migration was observed in adipocytes. *$P < 0.05$ and ***$P < 0.001$.

To characterize the phenotype of adipocyte postexposure to hypertonic medium, we further culture cells under standard culture medium to quantify their colony formation ability (Fig. 3A). Of the adipocytes exposed to hypertonic medium, 19.9 ± 5.4% are found to be capable of forming colonies with a population larger than 50 cells, whereas less than 2% of adipocyte postexposure to isotonic medium form colonies (Fig. 3D). These human adipocyte–derived cells are capable of undergoing myogenesis (Fig. 3, E and F), osteogenesis (Fig. 3, G and H, and fig. S1, C and D), adipogenesis (Fig. 3, I and J), and chondrogenesis (Fig. 3, K and L) via culture under respective differentiation induction media. The cells from colonies that are generated by hypertonic exposure retain self-renewing capability when cultured in MSC maintenance medium, with only a small portion of these cells exhibiting lipid droplet accumulation (less than 1% after 7 days) or alkaline phosphatase (ALP) expression (less than 3% after 7 days) (Fig. 3, G and H). Adipocytes derived from mouse MSCs show similar reduction in intracellular lipid droplet when cultured under hypertonic conditions and subsequently exhibit similar characteristics of colony formation and multipotent differentiation compared to human adipocytes (fig. S2). As adipocytes appear to adopt an MSC-like phenotype after culture in hypertonic medium, as marked by long-term self-renewal, multipotent differentiation capability, and serial clonogenicity, these cells are subsequently termed CiDAs. With these characteristics and the abundance of adipocytes in tissues, CiDAs may, thus, serve as a widely accessible resource for tissue engineering and regenerative medicine (*27*–*29*).

Multiple types of physical stresses, beyond elevated osmotic pressure, accompany tumor growth and progression (*12*, *21*), notably mechanical compression and increased matrix rigidity. To test whether these stressors can induce similar phenotypic changes in

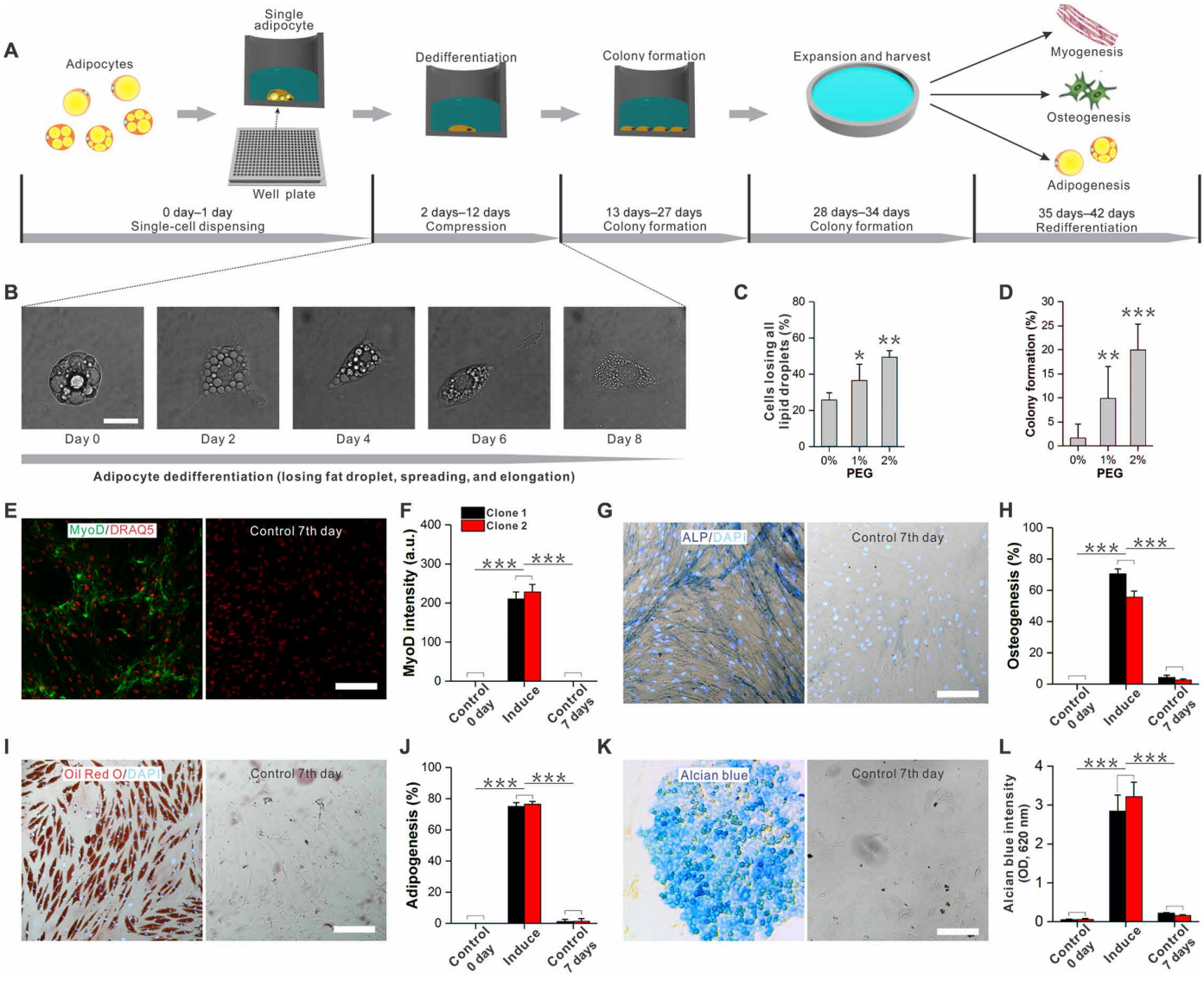

Fig. 3. Compression-induced dedifferentiation of single adipocytes. (**A**) Schematic outline of the compression treatment schedule. The adipocytes are individually isolated into 96-well plates and then compressed in hypertonic medium for 10 days and then incubated in expansion medium for another 2 weeks. The colonies of expanded dedifferentiated adipocytes are further redifferentiated into myoblasts, osteocytes, and adipocytes. (**B**) Images showing that the adipocytes gradually lose their lipid droplets, spread, and elongate under osmotic compression. Scale bar, 20 μm. (**C**) The dedifferentiation ratio is quantified as the ratio of adipocytes that lost all their obvious lipid droplets to the total number of initial adipocytes. The results show that osmotic compression increases the dedifferentiation ratio of adipocytes. Error bars represent SD ($n = 3$). (**D**) The colony formation ratio increases with increasing osmotic pressure. Error bars represent SD ($n = 3$). (**E** and **F**) Images (E) and quantification (F) of MyoD showing myogenic potential of CiDAs. Scale bar, 50 μm. Error bars represent SD ($n = 3$). (**G** and **H**) Images (G) and quantification (H) of ALP showing osteogenic potential of CiDAs. Scale bar, 50 μm. Error bars represent SD ($n = 3$). (**I** and **J**) Images (I) and quantification (J) of Oil Red O showing adipogenic potential of CiDAs. Scale bar, 50 μm. Error bars represent SD ($n = 3$). (**K** and **L**) Images (K) and quantification (L) of Alcian blue showing chondrogenic potential of CiDAs. Scale bar, 50 μm. Error bars represent SD ($n = 3$). OD, optical density. *$P < 0.05$, **$P < 0.01$, and ***$P < 0.001$.

adipocytes, we develop an approach to mechanically compress adipocytes cultured in three dimensions to mimic the mechanical compression in a native tissue during tumorigenesis. Density-sorted adipocytes are encapsulated in three-dimensional (3D) Matrigel covered by a porous membrane (fig. S3A). These adipocytes retain lipid droplets after 10 days of culture in 3D (fig. S3B). However, when mechanically compressed, achieved by the placement of a weight on the porous membrane (173 Pa, 40% engineering strain), 15.6 ± 2.7% of adipocytes lose all their lipid droplets over 10 days of culture (fig. S3, A and B), compared to 6.1 ± 2.2% of adipocytes cultured without compression. Furthermore, to test the effect of substrate stiffness on adipocyte phenotype, we culture density-sorted adipocytes on substrates with elastic moduli of either native breast tissue (200 Pa) or breast tumor (7 kPa) microenvironment. The dedifferentiation ratio of adipocytes is found to be higher on a stiff substrate as compared to that on a soft substrate; this effect is further augmented by the simultaneous application of osmotic pressure (fig. S3C), suggesting the synergistic nature of these different physical stimulations.

Overall, these results suggest that various types of physical stresses generated by tumor expansion may cooperatively drive the reprogramming of their surrounding adipocytes.

Genetic profiling of CiDAs

To further characterize CiDAs, we perform transcriptome profiling of established CiDA derived from mouse adipocytes using RNA sequencing (RNA-seq); we find that CiDAs are distinct from either adipocytes or MSCs, as shown by principal components analysis (Fig. 4A and fig. S4). CiDAs have elevated expression of pluripotency-associated genes such as *Sox2* and *Myc* (*30*), as well as cell cycling–associated genes (*31*) including *Cdkn1c*, *Cdkn2d*, *Ccne1*, *Cdc25a*, *Cdk1*, and *Cdc7*, as compared to MSCs (fig. S4). These results suggest that CiDAs are different from the MSCs. Furthermore, we also perform flow cytometry experiments of three different MSC-positive markers (CD90, CD73, and CD105) (*32*). We find that the CiDAs share the surface marker CD105 with the conventional MSCs but do not exhibit the expression of CD90 and CD73, which also confirm the difference between CiDAs and MSCs (fig. S5).

To determine the transcriptional signatures of adipocytes and CiDAs obtained through osmotic compression, we perform gene set enrichment analysis (GSEA) and find several dysregulated Kyoto Encyclopedia of Genes and Genomes (KEGG)/Gene Ontology (GO) pathways (*33*). Analysis of differently expressed genes with respect to overrepresented GO terms shows up-regulation of processes related to cell cycling and DNA replication (Fig. 4B and fig. S6), as well as down-regulation of processes related to cellular lipid metabolism and stimulus response (Fig. 4B and fig. S6). To explore the underlying molecular processes that potentially induce the adipocyte dedifferentiation, we examine several significantly up-regulated genes associated with stem cell pluripotency [including *sox2* and *myc*; (*30*)] and signal transduction [including Hippo signaling, bone morphogenetic protein (BMP) signaling, and Wnt signaling], according to the KEGG pathway database (Fig. 4C and fig. S7). Genes that overlap in these

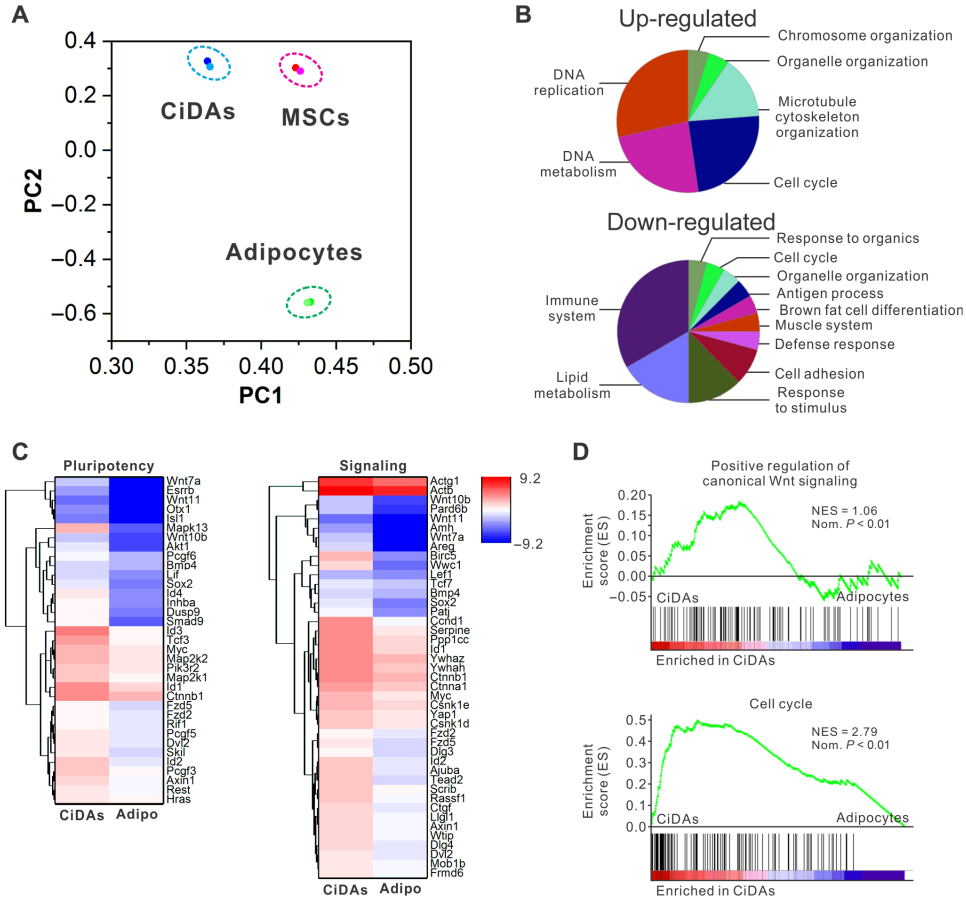

Fig. 4. Gene signatures of CiDAs as compared to adipocytes. (**A**) Principal components (PC) analysis of RNA-seq of CiDAs, MSCs, and adipocytes. Dots represent single colony. PC analysis results show that all those three cell types are distinct from each other and that CiDAs are more similar to MSCs as compared to adipocytes. (**B**) ClueGO analysis of up- and down-regulated genes in mouse adipocytes and CiDAs generated from these mouse adipocytes. RNA-seq is performed, and the significantly expressed genes are subsequently analyzed using ClueGO. The pie charts show the enriched groups represented by the most significant terms. The sizes of the sections correlate with the number of terms included in the corresponding group. The key up-regulated pathways (top) in CiDAs compared to the original adipocytes are mainly associated with cell cycling and DNA replication; the key down-regulated pathways (bottom) are mainly associated with cellular lipid metabolism and response to stimulus. (**C**) Up-regulated genes in CiDAs associated with cell pluripotency (left) and signaling transductions (right), including Hippo pathway, BMP pathway, and Wnt pathway, according to the KEGG pathway database. (**D**) GSEA enrichment plot of the KEGG/GO pathway of CiDAs compared to adipocytes. Genes show significant enrichment in cell cycle (bottom) and canonical Wnt signaling pathway (top). The top portion of the figure plots the enrichment score (ES) for each gene, whereas the bottom portion of the plot shows the value of the ranking metric moving down the list of ranked genes. NES, normalized ES; Nom., nominal.

two categories are considered to interconnect these two functional processes; we find 13 overlapping genes, all of which are canonical Wnt signaling–related genes such as *Wnt7a*, *Myc*, *Dvl2*, *Fzd5*, *Bmp4*, and *Sox2* (*34*, *35*), as shown in Fig. 4C. Consistent with significantly up-regulated genes, GSEA also shows a significant enrichment of cell cycling pathway and canonical Wnt signaling pathway in CiDAs as compared to adipocytes without compression (Fig. 4D).

Wnt/β-catenin signaling is a key regulator of compression-induced dedifferentiation of adipocytes

The canonical Wnt/β-catenin pathway is known to play a prominent role in relaying information from extracellular signals during adipogenesis (*36*). Activation of this pathway has been shown to negatively regulate precursors' commitment and differentiation along the adipocyte lineage (*37*) and induce dedifferentiation of mature adipocytes (*38*, *39*). Given the importance of the Wnt/β-catenin pathway in adipocyte dedifferentiation, we assess its activity in and importance to CiDA generation. Western analysis of β-catenin in mouse adipocytes exposed to hypertonic media reveals a positive correlation between hypertonicity and cytosolic β-catenin accumulation (Fig. 5A). Consistently, quantitative reverse transcription polymerase chain reaction (qRT-PCR) assays of Wnt target genes (*Axin2*, *Sp5*, *Sox2*, and *Myc*) confirm the downstream elevated Wnt signaling (fig. S8). Furthermore, immunostaining of β-catenin indicates increased nuclear colocalization upon osmotic compression (Fig. 5, B to D). To assess whether activation of the Wnt/β-catenin pathway is required for osmotic pressure–induced adipocyte dedifferentiation, adipocytes in isotonic or hypertonic media are exposed to IWP2, a porcupine inhibitor that blocks the secretion of Wnt ligands. Inhibition of Wnt/β-catenin signaling resulting from IWP2 exposure significantly reduces the dedifferentiation ratio of mouse adipocytes under osmotic compression (400 mosmol), partially restoring lipid droplet accumulation. When canonical Wnt/β-catenin signaling is rescued via addition of the exogenous Wnt3a ligand, compression-induced dedifferentiation is recovered (Fig. 5, E and F). Moreover, when Wnt/β-catenin signaling is enhanced by exposing adipocytes to exogenous Wnt3a ligand in the absence of IWP2 under isotonic conditions, the dedifferentiation ratio of mouse adipocytes is increased (Fig. 5, E and F). In addition, application of osmotic compression in combination with Wnt ligand stimulation further elevates adipocyte dedifferentiation compared to exposure to Wnt ligand or osmotic compression alone (Fig. 5, E and F). Together, these findings indicate that Wnt/β-catenin signaling mediates adipocyte dedifferentiation induced by physical compression.

CiDAs promote mammary tumor progression in xenograft mice model

To investigate the physiological consequences of compression-driven adipocyte dedifferentiation on tumor progression, we establish a xenograft model via subcutaneous injection of an mCherry-labeled human mammary adenocarcinoma cell line, MDA-MB-231, and CiDA derived from human adipocytes, either alone or in combination, into NOD/SCID/IL2γ$^{-/-}$ (NSG) mice (Fig. 6A). Coinjection of MDA-MB-231 with CiDAs yields a larger tumor than tumor cells alone over a 4-week period, as quantified by both tumor size and mass (Fig. 6, B and C). To assess the contribution to tumor formation due to MDA-MB-231 cells alone, the total fluorescence intensity of mCherry is measured and found to correlate with tumor size and mass measurements (Fig. 6, D and E). In addition, injection of CiDAs alone forms neither tumors nor teratomas (Fig. 6C).

To study the contribution of the CiDAs in promoting tumor growth, we conduct immunohistochemical analysis on xenograft tumor cross section and stained for α-smooth muscle actin (α-SMA),

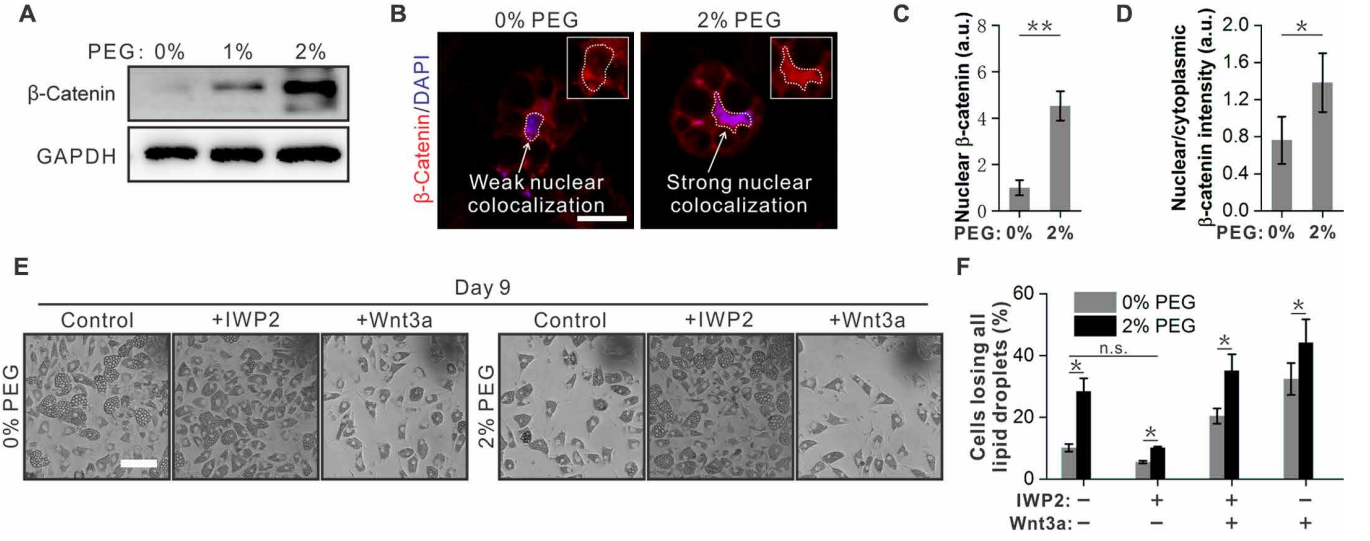

Fig. 5. CiDAs via modulating Wnt/β-catenin signaling. (**A**) Western blot analysis shows that osmotic compression increases the level of cytosolic β-catenin. Three independent experiments are performed to confirm the consistency of the results. GAPDH, glyceraldehyde-3-phosphate dehydrogenase. (**B**) Immunostaining shows that more β-catenin is accumulated in the nucleus upon osmotic compression. Scale bar, 20 μm. (**C**) Nuclear β-catenin is increased under osmotic compression quantified from the immunostaining in (B). Error bars represent SD ($n = 90$ cells derived from three independent experiments for each condition). (**D**) The ratio of nuclear to cytoplasmic β-catenin is increased under osmotic compression. Error bars represent SD ($n = 90$ cells derived from three independent experiments for each condition). (**E**) Bright-field images show the CiDAs in the control condition, or with IWP2 to inhibit the secretion of endogenous Wnt ligands, or with additional exogenous Wnt3a ligand, respectively. (**F**) Inhibition of Wnt/β-catenin signaling using IWP2 suppresses the compression-induced adipocyte dedifferentiation. Activation of Wnt/β-catenin signaling using additional exogenous Wnt3a ligand further increases dedifferentiation ratio of adipocytes both with and without osmotic compression. Error bars represent SD ($n = 3$). *$P < 0.05$ and **$P < 0.01$.

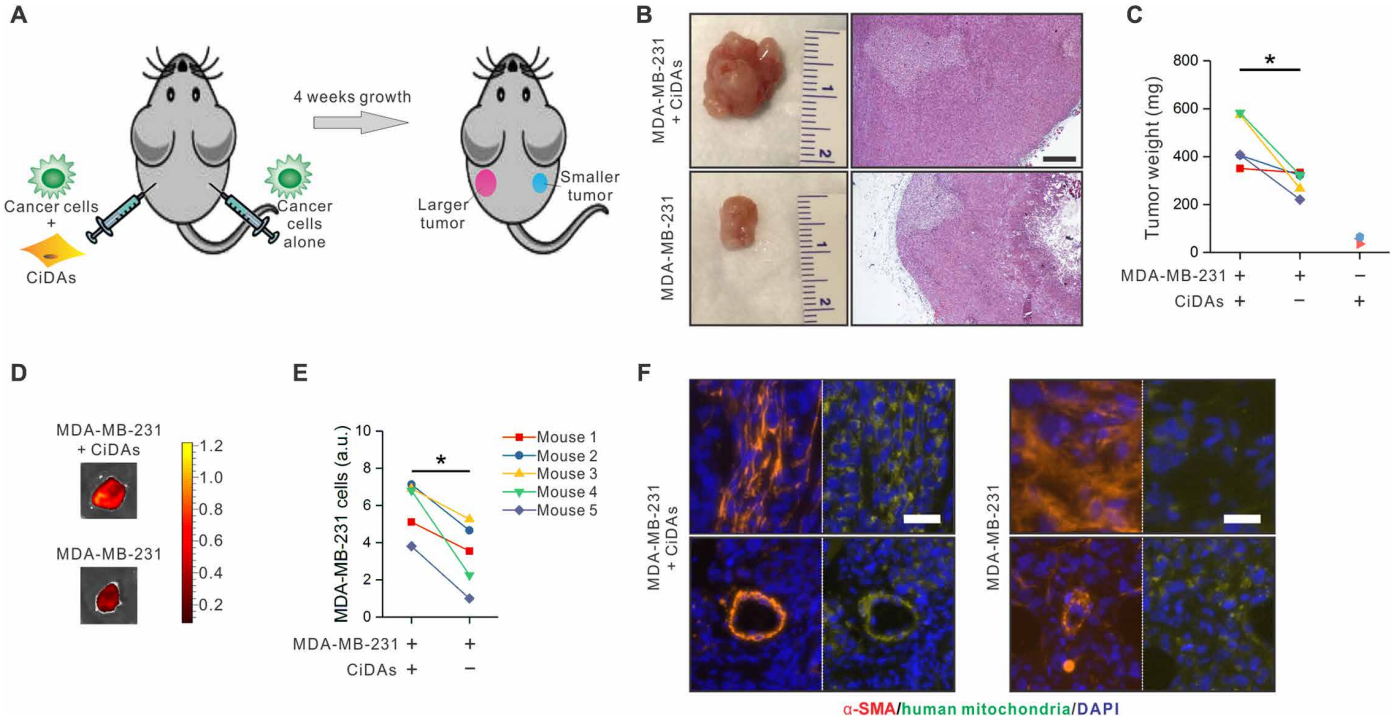

Fig. 6. CiDAs enhance tumor growth in a xenograft model. (**A**) Schematic illustration of coinjection of MDA-MB-231 cells and CiDAs or MDA-MB-231 cells alone. (**B**) Images show that the larger size of the tumor resulted from coinjection of MDA-MB-231 cells with CiDAs, compared with from tumor cells alone. Scale bar, 600 μm. (**C**) The weight of tumors that resulted from the coinjection is significantly larger than those from tumor cells alone. Different symbols represent different mice. The soft tissue explants generated from injected CiDAs alone are much smaller than the tumors generated. (**D** and **E**) Fluorescence intensities of tumors that resulted from coinjection of mCherry-labeled MDA-MB-231 cells with CiDAs are larger than those from injected mCherry-labeled MDA-MB-231 cells alone. (**F**) Immunofluorescence images show that α-SMA levels are greater in the explants that resulted from coinjection of CiDAs and MDA-MB-231 cells as compared with those from MDA-MB-231 cells alone. The α-SMA expression colocalizes with human mitochondria staining in the explants that resulted from coinjection of CiDAs and MDA-MB-231 cells, which indicates that these cells expressing α-SMA originate from CiDAs. Vascular development by CiDA-derived α-SMA–positive cells has been observed in the coinjected tumor rather than in the tumor from MDA-MB-231 cells alone. Scale bar, 30 μm. *$P < 0.05$. Photo credit: Angelo Mao, Harvard University.

a marker to identify myofibroblasts that are known to modulate tumor progression (*40*) by vascular development (*41*), ECM stiffening (*21*), and production of host-derived proangiogenic factors (*42*). The intensity of α-SMA is increased in tumors originating from coinjection of CiDAs with tumor cells as compared to that from tumor cells alone (Fig. 6F). Staining of human mitochondria shows colocalization with α-SMA, confirming that the de novo–generated α-SMA–positive cells are derived from the injected CiDAs and not host murine cells (Fig. 6F). Furthermore, vascular development by CiDA-derived α-SMA–positive cells in coimplanted tumors is observed but absent in tumors developed from MDA-MB-231 cells alone (Fig. 6F). As tumors coinjected with CiDAs exhibit an increased growth rate and the presence of intratumoral and peritumoral CiDA-derived myofibroblasts, we hypothesize that CiDAs exposed to the tumor microenvironment differentiate into myofibroblasts and accelerate tumor progression. In vitro, CiDAs are capable of differentiation into myofibroblasts upon exposure to transforming growth factor–β (TGF-β) or tumor-conditioned medium (TCM) (fig. S9, A to L) and, moreover, promote MDA-MB-231 proliferation in coculture (fig. S9, P to S). Adipocytes can be directly induced to adopt a myofibroblast phenotype with the application of osmotic compression and TGF-β stimulation together, in which the loss of lipid droplets and α-SMA induction occur simultaneously (fig. S9, M to O). Together, these results suggest that physical stresses generated by tumor growth may induce dedifferentiation of neighboring adipocytes, which subsequently further promote the growth of tumors via adoption of a myofibroblast phenotype.

DISCUSSION

Because of the consistent reporting of higher ECM stiffness, stresses, and osmotic compression in the tumor microenvironment (*12*–*17*, *43*, *44*), the role of physical properties of the microenvironment in tumor progression has garnered significant attention recently. These properties are primarily caused by tumor progression and characterized by increased ECM deposition, fiber alignment, and cross-linking, all of which promote tumor progression and malignancy (*13*, *17*). Here, we explore the effect of these physical hallmarks of the tumor microenvironment on adipocytes that are abundant in the breast stroma and their interaction with the cancer cells. We demonstrate that osmotic pressure, mechanical compression, and increased substrate stiffness can individually and synergistically drive reprogramming of adipocytes into multipotent cells, termed CiDAs here. We then show that CiDAs can significantly enhance the proliferation of human mammary adenocarcinoma MDA-MB-231 cells both in vitro and in a xenograft model by undergoing differentiation into tumor-friendly myofibroblast due to the presence of TGF-β in the cancer microenvironment. This observation of enhanced tumor growth in the presence of myofibroblast is consistent with previous studies (*21*, *40*, *41*, *45*).

Another aspect of the present work is a new strategy to induce cellular reprogramming of adipocytes into multipotent cells termed CiDAs only mediated by local physical stresses. CiDAs are capable of long-term self-renewal and serial clonogenicity (including osteogenesis, adipogenesis, myogenesis, chondrogenesis, and myofibrogenesis) without forming teratomas. This reprogramming of adipocytes is consistent with several recent studies on the dedifferentiation of committed cells into body stem cells in other tissues (*46*), such as intestine (*47*), neuron (*48*), and airway (*49*), and together highlights the cellular plasticity of adult tissues. Moreover, this physical reprogramming of adipocytes suggests a previously unknown opening of cellular reprogramming that could be important for understanding transdifferentiation in tissues. Mechanical induction of reprogramming, reported in this paper, leads to adipocytes undergoing a series of changes, which ultimately result in cells acquiring multipotency or stemness. The hallmark of adipocyte reprogramming is the loss of adipose lineage–specific transcripts and gain of stem cell–specific transcripts. We observe the reduction of genes associated with lipid metabolism, while the proliferative and pluripotent genes (such as *Sox2* and *Myc*) increases. We identify that canonical Wnt/β-catenin pathway signaling, which has been suggested to be mechanosensitive, mediates this adipocyte dedifferentiation induced by physical compression. This is consistent with previous studies showing that activation of this pathway negatively regulates precursors' commitment and differentiation along the adipocyte lineage (*37*) and induces dedifferentiation of mature adipocytes (*38*, *39*). The upstream mechanoregulators of Wnt/β-catenin signaling could be the changes of the intracellular crowdedness (*27*, *43*) or the deformation of nucleus (*50*). Our work, together with other previous research (*51*–*53*), highlights the unique capability of physical cues in activating or promoting cell reprogramming/dedifferentiation, which adds an extensive complexity to the native multicellular ecosystems. Last, we anticipate that our results can provide an entry point for understanding how the physical interplays between adipocytes and cancer cells affect the evolution of tumor ecosystems and potentially facilitate a wide range of engineering approaches.

MATERIALS AND METHODS

Cell culture

Clonally derived mouse MSCs (OP9) purchased from the American Type Culture Collection (ATCC) were expanded subconfluently in Minimum Essential Medium Eagle Alpha Modification media supplemented with 20% fetal bovine serum and 1% penicillin/streptomycin (complete αMEM). Viability was assessed by cells with calcein acetoxymethyl and ethidium homodimer-1 (Invitrogen, Eugene, OR) or trypan blue exclusion (Beckman Coulter). Subcutaneous primary human adipocytes were purchased from Lonza and cultured at subconfluence in Preadipocyte Growth Medium-2 (Lonza) following the manufacturer's instructions (passage 0). A passage number up to 6 was used for the experiments. MDA-MB-231 cells were obtained from the ATCC and cultured in Dulbecco's modified Eagle's medium supplemented with 10% fetal bovine serum (complete DMEM).

Osmotic stress

Hyperosmotic stress was applied by adding polyethylene glycol 300 (PEG 300) to isotonic culture medium. The correlation between molarity and osmolality for solutions of PEG in water was taken from previous measurement (*54*). The actual osmotic pressure applied to cells was calculated by summing up the osmotic pressures of PEG and isotonic medium (325 mosmol) and was further validated by measurement using a micro-osmometer (model 3300, Advanced Instruments Inc.). Cells were incubated for 10 min at 37°C and 5% CO_2 in PEG-supplemented culture medium solution. The cell size and mechanics achieved equilibration within 2 min after adding PEG 300 based on previous studies (*27*). In addition to osmolarity, we also calculated the corresponding osmotic pressure when we added hypertonic medium using van't Hoff's equation $\pi = cRT$. In the equation, π represents the osmotic pressure in pascals, c represents the molar concentration of the solutes, T represents the absolute temperature, and R represents the gas constant. As calculated, 2% PEG 300 used in hypertonic medium induced an additional 171.9 kPa, while 1% PEG 300 induced an additional 85.9 kPa.

Adipogenic differentiation

To induce adipogenesis, OP9 mouse MSCs (mMSCs) were supplemented with αMEM (Gibco) supplemented with 15% KnockOut Serum Replacement (Gibco) (*55*). Human preadipocyte adipogenesis was induced via culture in Preadipocyte Growth Medium-2 (Lonza) supplemented with SingleQuots (Lonza) consisting of insulin, dexamethasone, indomethacin, and 3-isobutyl-1-methylxanthine, as per the manufacturer's instructions (https://bioscience.lonza.com/lonza_bs/CH/en/document/download/28861). In experiments where a purer population of differentiated cells was desired, cells were trypsinized and sorted by density. Briefly, detached adipocytes were ceiling cultured in a flask for bulk cell experiments and in wells for single-cell experiments. For histological analysis of adipogenesis specification, cells were fixed after 10 days of culture with 4% paraformaldehyde (Thermo Fisher Scientific) in phosphate-buffered saline (PBS) (Gibco) with 0.1% Triton X-100 (Sigma-Aldrich) for 30 min at 25°C and washed in PBS. Neutral lipid accumulation was visualized by Oil Red O (Abcam) staining as a functional marker for adipogenesis.

Myogenic differentiation

To induce myogenesis, the CiDAs were cultured with myogenic medium for more than 10 days in complete DMEM supplemented with 5% horse serum (HS) (Gibco), 0.1 μM dexamethasone (Sigma-Aldrich), and 50 μM hydrocortisone (Sigma-Aldrich), cycling every 2 days (*56*–*58*). To assess myogenesis efficiency, immunofluorescence staining of the muscle-specific transcription factor MyoD1 was performed. Cells were rinsed twice with PBS, fixed with 4% paraformaldehyde for 20 min, and washed three times with PBS. The cells were incubated with 3% hydrogen peroxide (Sigma-Aldrich) in PBS for 10 min to quench endogenous peroxidase enzyme activity, and nonspecific sites were blocked by incubation in blocking buffer (PBS, 10% HS, and 0.1% Triton X-100) for an additional 60 min. The cells were washed three times for 5 min each in blocking buffer and incubated for 1 hour in blocking buffer containing anti-MyoD1 (Abcam). The cells were rinsed extensively in blocking buffer and the secondary antibody donkey anti-rabbit Alexa Fluor 488 (Thermo Fisher Scientific) according to the manufacturer's manual.

Osteogenic differentiation

To induce osteogenesis, the CiDAs were cultured with complete DMEM supplemented with 10 mM β-glycerophosphate and 250 μM L-ascorbic acid, cycling every 2 days (*59*). mMSCs were fixed after 3 days of culture, stained, and permeabilized with Triton X-100. To assess ALP activity, mMSCs were fixed 6 days after osteogenic induction and stained with ELF 97 (Thermo Fisher Scientific) following the manufacturer's instructions.

Myofibrogenic differentiation

To induce myogenesis, the CiDAs were cultured with either myofibrogenic medium or TCM. Myofibrogenic medium was made by supplementing complete DMEM with TGF-β (2 ng/ml; Abcam) (*21*, *60*). TCM was harvested from the MDA-MB-231 cells. After MDA-MB-231 reached confluence, fresh medium was added and then harvested after 24 hours. To assess the myofibrogenesis ratio, immunostaining of α-SMA was performed. Cells were incubated with 3% hydrogen peroxide in PBS for 10 min to quench endogenous peroxidase enzyme activity, and nonspecific sites were blocked by incubation in blocking buffer (PBS, 10% HS, and 0.1% Triton X-100) for an additional 60 min. The cells were washed three times for 5 min each in blocking buffer and incubated for 1 hour in blocking buffer containing anti–α-SMA (Abcam). The cells were rinsed extensively in blocking buffer and subsequently incubated with donkey anti-rabbit Alexa Fluor 488 secondary (Thermo Fisher Scientific).

Morphology analysis and quantification of dedifferentiation ratio of adipocytes in bulk experiments

After seeding adipocytes, up to nine areas were randomly selected, and their locations were marked using Leica SP8 confocal software. In each well of different experimental conditions, nine fields of view were collected using Leica SP8 confocal software at randomly dispersed locations. Practically, the area of the well was divided into a 3 × 3 subarea, and each field of view was randomly selected and recorded in each corresponding subarea. Cells in these nine fields of view were picked up for the following measurements. Every 2 days, the images of the same selected locations were obtained using a Leica SP8 confocal microscope. Individual cells were tracked in each image every 2 days over 10 days. The dedifferentiation ratio was quantified as the number of adipocytes that lost all visible lipid droplets over the total starting number of adipocytes. The aspect ratios of individual adipocytes were calculated as the length of the longest axis of each cell divided by the length of its perpendicular axis. The lipid sizes in adipocytes were measured as the diameter of individual lipid droplets. Images were analyzed using ImageJ.

Adipocyte dedifferentiation ratio (the ratio of cells losing all lipid droplets)

The intracellular lipid droplet is one of the most widely used markers for adipocyte. Here, the ratio of cells losing the obvious intracellular lipid droplets was defined as the dedifferentiation ratio of adipocyte. We measured the size of the lipid droplets from the bright-field images using TrackMate in ImageJ to measure the size of the spherical droplet, and if it was either smaller or equal to ~1 μm, then we say that the cells have lost the lipid droplets. Previous studies (*38*, *39*, *61*–*64*) have made similar arguments about the adipocytes losing lipid droplets based on just observation; however, we followed a more quantitative approach based on the size of the lipid droplet, making the process more consistent and deterministic. For each dish, a field of view of 10 mm by 7 mm was recorded using a Leica SP8 confocal microscope with the function called tiling, in which the confocal microscope automatically imaged everywhere in that predefined field and stitched images to form a final image. The field of view had a comparable size to the whole area of culture dish (40%), which was selected basically at the center of the dish. For each condition, more than 1000 cells were counted for the final calculation in the selected field.

Single adipocyte colony formation assay

The adipocytes sorted by density were diluted and isolated into each well of the 96-well plate according to the nature of Poisson distribution. Because of the lower density of adipocytes in comparison to the culturing medium, the adipocytes floated in the top layer of the medium. Then, we turned the well plate upside down to allow the adipocytes to fully attach to the well plate. After overnight incubation, the well plates were flipped back, and the medium was exchanged with hypertonic medium to induce osmotic compression. Then, individual wells containing exactly one adipocyte were confirmed under a microscope and marked. The hypertonic medium was exchanged every 2 days. After 10 days of culturing, the well plates were imaged under the microscope to find out the well-contained cells that had already lost all their obvious lipid droplets. Then, the medium in each well was exchanged with MSC expansion medium, which was exchanged every 2 days for 2 weeks of culture. Last, the wells containing a cell colony (more than 50 cells) were counted. The colony formation ratio was calculated by the ratio of wells containing colonies to the total number of wells containing single adipocytes at the beginning.

Characterization of CiDA proliferation and migration

To assess proliferation, adipocytes, MSCs, and CiDAs were seeded in well plates at a consistent number. We quantified the cell numbers before and after 2 days of culturing. The fold increase of the cell number was calculated to indicate their proliferation capability. After CiDAs, MSCs and adipocytes were attached on the well plate, and videos were taken on a Leica SP8 confocal microscope for 24 hours. The total length cell migration was measured, and the average migration speed was calculated for comparison.

Fabrication of polyacrylamide gel substrate

Polyacrylamide gels of various stiffnesses were fabricated on 35-mm glass-bottom culture dishes (MatTek, Ashland, MA). Briefly, the bottom no. 1 coverslip was aminosilanized to enable polyacrylamide attachment. Gel stiffness was varied by adjusting the concentrations of the monomer acrylamide (Bio-Rad) and the cross-linker bis-acrylamide (Bio-Rad, Hercules, CA). Gels with a shear modulus of 7 kPa consisted of 7.5% acrylamide and 0.1% bis-acrylamide, while those of 200 Pa consisted of 3% acrylamide and 0.08% bis-acrylamide. The polymerization was initiated by the addition of ammonium persulfate and *N*,*N*,*N*′,*N*′-tetramethylethylenediamine (TEMED). Immediately after initiating polymerization, a controlled volume was added to the glass-bottom dishes. Then, another unmodified coverslip was placed on top to cover the polymerizing gel to ensure a flat gel surface. After polymerization, the top coverslip was removed, and the gel surface was functionalized with collagen I (0.1 mg/ml; Invitrogen; Cohesion Technologies, Palo Alto, CA) using the sulfo-SANPAH (Pierce Biotechnology, Rockford, IL) activation method (*65*). Collagen attachment and uniformity were confirmed using fluorescent collagen (Elastin Products, Owensville, MO). The gel thickness was found to be 70 to 100 μm by confocal microscopy. The shear modulus G' of macroscopic polyacrylamide gel samples was measured using a rheometer (AR-G2; TA Instruments, New Castle, DE).

Mechanical compression of cells cultured in 3D Matrigel

To mechanically compress cells in 3D culture, adipocytes were encapsulated in Matrigel covered by a porous membrane. A weight was placed on the top glass slide to introduce a vertical compression of

173 Pa. Then, the adipocytes were cultured with either isotonic or hypertonic stem cell maintenance medium for 10 days.

Quantitative reverse transcription polymerase chain reaction

The RNA of treated adipocytes was extracted on the ninth day after compression. RNA extraction was performed using TriPure Isolation Reagent (Roche) according to the manufacturer's instructions. Complementary DNA (cDNA) was synthesized from 1 μg of RNA using the iScript Select cDNA Synthesis Kit (Bio-Rad). Real-time qRT-PCR was carried out with the primer sets listed below using iQ SYBR Green Supermix (Bio-Rad) with the Applied Biosystems 7900HT System. The expression of genes of interest was normalized to that of glyceraldehyde-3-phosphate dehydrogenase (*GAPDH*) in all samples. The primers used for PCR amplification are as follows: *Sox2*, 5′-GGTTACCTCTTCCTCCCACTCCAG-3′ (forward) and 5′-TCACATGTGCGACAGGGGCAG-3′ (reverse); *GAPDH*, 5′-CCATGTTTGTGATGGGTGTGAACC-3′ (forward) and 5′-TGTGAGGGAGATGCTCAGTGTTGG-3′ (reverse); *Axin2*, 5′-TAGGCGGAATGAAGATGGAC-3′ (forward) and 5′-CTGGTCACCCAACAAGGAGT-3′ (reverse); *Sp5*, 5′-TCCAGACCAACAAACACACCA-3′ (forward) and 5′-AGTTTGCCGCTACCCAATCA-3′ (reverse); *Myc*, 5′-CAGCTGCTTAGACGCTGGATT-3′ (forward) and 5′-GTAGAAATACGGCTGCACCGA-3′ (reverse).

Gene expression profiling using RNA-seq

The RNA was extracted on the 25th day (10 days of osmotic compression and 14 days of colony expansion) for RNA-seq. Library construction of digital gene expression sequencing generated tags with 21 base pairs (bp) from the 3′ ends of each transcript, and these tags were used to represent the expression levels of transcripts. Sequencing libraries were prepared following the established protocols (*66*). Briefly, after extraction of total RNA, double-stranded cDNA was synthesized from RNA using oligo$(dT)_{18}$ beads (Invitrogen). Afterward, cDNA product was digested with Nla III and then linked to the first sequencing adapter. The product of ligation was digested with Mme I and linked to the second adapter. Then, the double adapter-flanked tags were amplified, and the products were purified using Spin-X filter columns. Last, mRNA libraries were sequenced on a BGI-500 system following the manufacturer's protocol.

Analysis of sequencing data

Details of primary analysis of sequencing data were described in a previous publication (*67*). Briefly, all the 17-bp DNA sequence next to Nla III restriction sites on a mouse reference genome along with the 4-bp CATG recognition site were extracted and concatenated as a new reference. Tags were mapped to construct reference using SOAP2, allowing no more than one mismatch. Normalized TPM (transcripts per million clean tags) values and fold change (absolute value of $\log_2$ ratio, either CiDAs versus mMSCs or CiDAs versus adipocytes) were calculated using uniquely mapping tags. Subsequently, candidates for differentially expressed genes were identified using the statistical test developed by Audic and Claverie (*68*), and a *P* value for each gene was calculated for each of the 10 cancer-normal pairs. We then calculated the false discovery rate (FDR) to control the proportion of false-positive results. Differential expression FDRs were calculated according to the method proposed by Storey and Tibshirani (*69*) implemented in the R package *q* value (version 2.6.0). The differently expressed genes shown in Fig. 4C were selected as those genes with an FDR of <0.001 between the two categories as indicated in the figure. The same group of genes with an FDR of <0.001 was used for GO enrichments.

For the comparison with RNA-seq data, statistical significance of overlapping was calculated using hypergeometric test by R (www.R-project.org). A two-way unsupervised hierarchical clustering was performed using average linkage and uncentered Pearson correlation metric by Gene Cluster 3.0, and results were visualized using TreeView.

For pathway enrichment, we took all the recurrently deregulated genes as input for Cytoscape with ClueGO plug-in. To mine out the relevant genes, we performed leading edge analysis of GSEA tool (*33*). GSEA v3.0 was used to generate (Fig. 4D and figs. S4C and S6), calculate the enrichment score (ES), and test the hypothesis. Briefly, the genes from mRNA expression profiles were ordered in a ranked list L according to their differential expression between the classes. Given an a priori defined set of genes S, such as GO category, we then determined whether the membrane of gene category was randomly distributed throughout L or primarily found at the top of bottom. The software calculated an ES that reflects the degree to which a gene set S was overrepresented at the extremes of the entire ranked list of functional gene set L. The score was calculated by walking down the list L, increasing a running-sum statistic when encountering a gene in S and decreasing it when encountering genes not in S. The ES was the maximum deviation from zero encountered in the random walk; it corresponded to a weighted Kolmogorov-Smirnov–like statistic. We further estimated the statistical significance (nominal *P* value) of the ES by using an empirical phenotype-based permutation test procedure that preserved the complex correlation structure of the gene expression data. When an entire database of gene sets was evaluated, we adjusted the estimated significance level to account for multiple hypothesis testing. We normalized the ES for each gene set to account for the size of the set, yielding a normalized ES. Core genes ranked at both ends on the heat map of each gene set were most significantly discrepant between either CiDAs and mMSCs or CiDAs and adipocytes. In our study, all the deregulated genes were interrogated in the gene sets by the KEGG database and GO database.

Coculturing of MDA-MB-231 cells and CiDAs in vitro

mCherry-transduced MDA-MB-231 cells were cultured either alone or with equal numbers of CiDAs. After 2 days of culture, the number of MDA-MB-231 cells, the total intensity of mCherry, and the total area of MDA-MB-231 cells were quantified to assess the impact of CiDAs on the growth of MDA-MB-231 cells.

Animal experiments

All animal experiments were performed in accordance with the institutional guidelines approved by the ethical committee from Harvard University. Animals were housed and provided with food and water ad libitum. For xenograft experiments, mCherry-transduced MDA-MB-231 were subcutaneously injected alone or together with an equal number of CiDAs into NOD.Cg-*Prkdc*^{scid} *Il2rg*^{tm1Wjl}/SzJ or NSG mice between 3 and 4 weeks of age. Matrigel was used as a carrier to increase localization of cells at the side of injection. Animals were euthanized after 4 weeks, and tumors were dissected out, weighed, and imaged using the IVIS Spectrum In Vivo Imaging System (PerkinElmer).

Staining procedure

For immunocytochemistry, formalin-fixed cells were rinsed with 0.05% Triton X-100 in PBS (PBS-1x) followed by incubation with

2% bovine serum albumin (BSA) in PBS-1x (PBS-1x/BSA) for blocking. Afterward, the cells were incubated with the desired primary antibody diluted in PBS-1x/BSA overnight at 4°C. Following two washes in PBS-1x, samples were incubated with secondary antibodies diluted in PBS-1x/BSA for 1 hour at room temperature. The following primary antibodies were used: rabbit anti-mouse MyoD (Invitrogen), rabbit anti-human MyoD (Invitrogen), and rabbit anti-mouse α-SMA (Abcam). 4′,6-Diamidino-2-phenylindole (DAPI) was used as a nuclear counterstain, and Alexa Fluor 488 or 568 served as the secondary antibody (all from Invitrogen). Imaging was performed by epifluorescence microscopy, consisting of a Xenon lamp, an Axio Zoom V16 microscope, and a Hamamatsu Flash 4.0 v3.

Western blot analysis

Western blotting was performed using standard protocols. We used primary antibodies against α-SMA, β-actin, and GAPDH. We used goat antibodies to mouse and rabbit conjugated with horseradish peroxidase as secondary antibodies (Jackson ImmunoResearch) and developed the blots using enhanced chemiluminescence (Dura, Pierce).

3D volume measurement

3D stained cell images were obtained using 63×/1.2–numerical aperture water immersion lens on a confocal microscope (Leica SP8, Germany). Cells were randomly picked to be imaged. In each well of different experimental conditions, nine fields of view were collected using a Leica SP8 confocal microscope at randomly dispersed locations. Practically, the area of well was divided into a 3 × 3 subarea, and each field of view was randomly selected and recorded in each corresponding subarea. Cells in these nine fields of view were picked for the following measurements. The optical cross sections were recorded at 0.15-μm z axis intervals to show intracellular, nuclear, and cortical fluorescence. The x-y pixel size was chosen to be comparable to the z axis interval to achieve better voxel resolution and better deconvolution results. The 3D image was deconvolved using Huygens Software before 3D visualization. 3D visualization was carried out using ImageJ, Amira software, and LAS X 3D Visualization from Leica. The volume of cells and cell nuclei were calculated by counting the voxel number after thresholding the stack using a custom MATLAB algorithm. The threshold was selected as the fluorescence intensity on the bottom interface of the cells that could be identified from the confocal reflection imaging. The confocal measurement of cell volume had been previously compared with measurement using atomic force microscopy and superresolution structured illustration microscopy, showing consistent results for both the cell height and cell volume (*27*, *70*).

Statistical analysis and sample information

Statistically significant differences between the means of two groups were assessed using Student's t test, whereas data containing more than two experimental groups were analyzed with a one-way analysis of variance (ANOVA) followed by Bonferroni's multiple comparisons test. All statistical analyses were performed in the Origin 9.0 software. $^{*}P < 0.05$, $^{**}P < 0.01$, and $^{***}P < 0.001$.

Data availability

All primary data will be included in the source data associated with each figure accompanying this paper. All other data that support the findings of this study are available from the corresponding author upon reasonable request.

SUPPLEMENTARY MATERIALS

Supplementary material for this article is available at http://advances.sciencemag.org/cgi/content/full/6/4/eaax5611/DC1

Fig. S1. Alizarin Red assays confirm the osteogenic differentiation of mouse CiDAs.
Fig. S2. Compression-induced dedifferentiation of single mouse adipocytes.
Fig. S3. Physical cues induced dedifferentiation of adipocytes.
Fig. S4. Comparison of gene expression between CiDAs and MSCs.
Fig. S5. Flow cytometry to test the potential surface markers of CiDA cells.
Fig. S6. GSEA enrichment plot of the KEGG/GO pathway of CiDAs compared to adipocytes.
Fig. S7. Up- and down-regulated genes in CiDAs compared to adipocytes.
Fig. S8. qRT-PCR analysis of Wnt target genes in adipocytes cultured with or without osmotic compression.
Fig. S9. In vitro myofibrogenesis of CiDAs promotes the growth of MDA-MB-231 cells.
Movie S1. Video shows that adipocyte gradually loses its intracellular lipid droplet in 10 days under osmotic compression.
Table S1. Reagent and resource.

View/request a protocol for this paper from *Bio-protocol*.

REFERENCES AND NOTES

1. N. McGranahan, C. Swanton, Clonal heterogeneity and tumor evolution: Past, present, and the future. *Cell* **168**, 613–628 (2017).
2. A. K. Casasent, A. Schalck, R. Gao, E. Sei, A. Long, W. Pangburn, T. Casasent, F. Meric-Bernstam, M. E. Edgerton, N. E. Navin, Multiclonal invasion in breast tumors identified by topographic single cell sequencing. *Cell* **172**, 205–217.e12 (2018).
3. S. K. Yeo, J.-L. Guan, Breast cancer: Multiple subtypes within a tumor? *Trends Cancer* **3**, 753–760 (2017).
4. J. Varga, F. R. Greten, Cell plasticity in epithelial homeostasis and tumorigenesis. *Nat. Cell Biol.* **19**, 1133–1141 (2017).
5. E. Lengyel, L. Makowski, J. DiGiovanni, M. G. Kolonin, Cancer as a matter of fat: The crosstalk between adipose tissue and tumors. *Trends Cancer* **4**, 374–384 (2018).
6. A. J. Hoy, S. Balaban, D. N. Saunders, Adipocyte–tumor cell metabolic crosstalk in breast cancer. *Trends Mol. Med.* **23**, 381–392 (2017).
7. O. C. Olson, D. F. Quail, J. A. Joyce, Obesity and the tumor microenvironment. *Science* **358**, 1130–1131 (2017).
8. A. J. Klil-Drori, L. Azoulay, M. N. Pollak, Cancer, obesity, diabetes, and antidiabetic drugs: Is the fog clearing? *Nat. Rev. Clin. Oncol.* **14**, 85–99 (2017).
9. J. O'Sullivan, J. Lysaght, C. L. Donohoe, J. V. Reynolds, Obesity and gastrointestinal cancer: The interrelationship of adipose and tumour microenvironments. *Nat. Rev. Gastroenterol. Hepatol.* **15**, 699–714 (2018).
10. C. A. Lyssiotis, A. C. Kimmelman, Metabolic interactions in the tumor microenvironment. *Trends Cell Biol.* **27**, 863–875 (2017).
11. M. E. Fernández-Sánchez, S. Barbier, J. Whitehead, G. Béalle, A. Michel, H. Latorre-Ossa, C. Rey, L. Fouassier, A. Claperon, L. Brullé, E. Girard, N. Servant, T. Rio-Frio, H. Marie, S. Lesieur, C. Housset, J.-L. Gennisson, M. Tanter, C. Ménager, S. Fre, S. Robine, E. Farge, Mechanical induction of the tumorigenic β-catenin pathway by tumour growth pressure. *Nature* **523**, 92–95 (2015).
12. H. T. Nia, H. Liu, G. Seano, M. Datta, D. Jones, N. Rahbari, J. Incio, V. P. Chauhan, K. Jung, J. D. Martin, V. Askoxylakis, T. P. Padera, D. Fukumura, Y. Boucher, F. J. Hornicek, A. J. Grodzinsky, J. W. Baish, L. L. Munn, R. K. Jain, Solid stress and elastic energy as measures of tumour mechanopathology. *Nat. Biomed. Eng.* **1**, 0004 (2016).
13. M. J. Mitchell, R. K. Jain, R. Langer, Engineering and physical sciences in oncology: Challenges and opportunities. *Nat. Rev. Cancer* **17**, 659–675 (2017).
14. R. Gutmann, M. Leunig, J. Feyh, A. E. Goetz, K. Messmer, E. Kastenbauer, R. K. Jain, Interstitial hypertension in head and neck tumors in patients: Correlation with tumor size. *Cancer Res.* **52**, 1993–1995 (1992).
15. P. A. Netti, L. T. Baxter, Y. Boucher, R. Skalak, R. K. Jain, Time-dependent behavior of interstitial fluid pressure in solid tumors: Implications for drug delivery. *Cancer Res.* **55**, 5451–5458 (1995).
16. C.-H. Heldin, K. Rubin, K. Pietras, A. Östman, High interstitial fluid pressure—An obstacle in cancer therapy. *Nat. Rev. Cancer* **4**, 806–813 (2004).
17. K. R. Levental, H. Yu, L. Kass, J. N. Lakins, M. Egeblad, J. T. Erler, S. F. T. Fong, K. Csiszar, A. Giaccia, W. Weninger, M. Yamauchi, D. L. Gasser, V. M. Weaver, Matrix crosslinking forces tumor progression by enhancing integrin signaling. *Cell* **139**, 891–906 (2009).
18. S. C. Wei, L. Fattet, J. H. Tsai, Y. Guo, V. H. Pai, H. E. Majeski, A. C. Chen, R. L. Sah, S. S. Taylor, A. J. Engler, J. Yang, Matrix stiffness drives epithelial–mesenchymal transition and tumour metastasis through a TWIST1–G3BP2 mechanotransduction pathway. *Nat. Cell Biol.* **17**, 678–688 (2015).
19. S. C. Wei, J. Yang, Forcing through tumor metastasis: The interplay between tissue rigidity and epithelial–mesenchymal transition. *Trends Cell Biol.* **26**, 111–120 (2016).
20. L. Przybyla, J. M. Muncie, V. M. Weaver, Mechanical control of epithelial-to-mesenchymal transitions in development and cancer. *Annu. Rev. Cell Dev. Biol.* **32**, 527–554 (2016).

21. E. M. Chandler, B. R. Seo, J. P. Califano, R. C. Andresen Eguiluz, J. S. Lee, C. J. Yoon, D. T. Tims, J. X. Wang, L. Cheng, S. Mohanan, M. R. Buckley, I. Cohen, A. Y. Nikitin, R. M. Williams, D. Gourdon, C. A. Reinhart-King, C. Fischbach, Implanted adipose progenitor cells as physicochemical regulators of breast cancer. *Proc. Natl. Acad. Sci. U.S.A.* **109**, 9786–9791 (2012).
22. J. E. Druso, C. Fischbach, Biophysical properties of extracellular matrix: Linking obesity and cancer. *Trends Cancer* **4**, 271–273 (2018).
23. B. R. Seo, P. Bhardwaj, S. Choi, J. Gonzalez, R. C. A. Eguiluz, K. Wang, S. Mohanan, P. G. Morris, B. Du, X. K. Zhou, L. T. Vahdat, A. Verma, O. Elemento, C. A. Hudis, R. M. Williams, D. Gourdon, A. J. Dannenberg, C. Fischbach, Obesity-dependent changes in interstitial ECM mechanics promote breast tumorigenesis. *Sci. Transl. Med.* **7**, 301ra130 (2015).
24. J. M. Petrosino, A. Leask, F. Accornero, Genetic manipulation of CCN2/CTGF unveils cell-specific ECM-remodeling effects in injured skeletal muscle. *FASEB J.* **33**, 2047–2057 (2018).
25. A. I. Caplan, All MSCs are pericytes? *Cell Stem Cell* **3**, 229–230 (2008).
26. F.-J. Müller, J. Goldmann, P. Löser, J. F. Loring, A call to standardize teratoma assays used to define human pluripotent cell lines. *Cell Stem Cell* **6**, 412–414 (2010).
27. M. Guo, A. F. Pegoraro, A. Mao, E. H. Zhou, P. R. Arany, Y. Han, D. T. Burnette, M. H. Jensen, K. E. Kasza, J. R. Moore, F. C. Mackintosh, J. J. Fredberg, D. J. Mooney, J. Lippincott-Schwartz, D. A. Weitz, Cell volume change through water efflux impacts cell stiffness and stem cell fate. *Proc. Natl. Acad. Sci. U.S.A.*, E8618–E8627 (2017).
28. S. K. Gupta, Y. Li, M. Guo, Anisotropic mechanics and dynamics of a living mammalian cytoplasm. *Soft Matter* **15**, 190–199 (2019).
29. Y. Li, F. Guo, Y. Hao, S. K. Gupta, J. Hu, Y. Wang, N. Wang, Y. Zhao, M. Guo, Helical nanofiber yarn enabling highly stretchable engineered microtissue. *Proc. Natl. Acad. Sci.* **116**, 9245–9250 (2019).
30. I.-H. Park, R. Zhao, J. A. West, A. Yabuuchi, H. Huo, T. A. Ince, P. H. Lerou, M. W. Lensch, G. Q. Daley, Reprogramming of human somatic cells to pluripotency with defined factors. *Nature* **451**, 141–146 (2008).
31. M. Malumbres, M. Barbacid, Cell cycle, CDKs and cancer: A changing paradigm. *Nat. Rev. Cancer* **9**, 153–166 (2009).
32. F.-J. Lv, R. S. Tuan, K. Cheung, V. Y. Leung, Concise review: The surface markers and identity of human mesenchymal stem cells. *Stem Cells* **32**, 1408–1419 (2014).
33. A. Subramanian, P. Tamayo, V. K. Mootha, S. Mukherjee, B. L. Ebert, M. A. Gillette, A. Paulovich, S. L. Pomeroy, T. R. Golub, E. S. Lander, J. P. Mesirov, Gene set enrichment analysis: A knowledge-based approach for interpreting genome-wide expression profiles. *Proc. Natl. Acad. Sci. U.S.A.* **102**, 15545–15550 (2005).
34. X. Lian, J. Zhang, S. M. Azarin, K. Zhu, L. B. Hazeltine, X. Bao, C. Hsiao, T. J. Kamp, S. P. Palecek, Directed cardiomyocyte differentiation from human pluripotent stem cells by modulating Wnt/β-catenin signaling under fully defined conditions. *Nat. Protoc.* **8**, 162–175 (2013).
35. A. Marson, R. Foreman, B. Chevalier, S. Bilodeau, M. Kahn, R. A. Young, R. Jaenisch, Wnt signaling promotes reprogramming of somatic cells to pluripotency. *Cell Stem Cell* **3**, 132–135 (2008).
36. I. Takada, A. P. Kouzmenko, S. Kato, Wnt and PPARγ signaling in osteoblastogenesis and adipogenesis. *Nat. Rev. Rheumatol.* **5**, 442–447 (2009).
37. S. E. Ross, N. Hemati, K. A. Longo, C. N. Bennett, P. C. Lucas, R. L. Erickson, O. MacDougald, Inhibition of adipogenesis by Wnt signaling. *Science* **289**, 950–953 (2000).
38. L. Bochet, C. Lehuede, S. Dauvillier, Y. Y. Wang, B. Dirat, V. Laurent, C. Dray, R. Guiet, I. Maridonneau-Parini, S. le Gonidec, B. Couderc, G. Escourrou, P. Valet, C. Muller, Adipocyte-derived fibroblasts promote tumor progression and contribute to the desmoplastic reaction in breast cancer. *Cancer Res.* **73**, 5657–5668 (2013).
39. B. Gustafson, U. Smith, Activation of canonical wingless-type MMTV integration site family (Wnt) signaling in mature adipocytes increases β-catenin levels and leads to cell dedifferentiation and insulin resistance. *J. Biol. Chem.* **285**, 14031 (2010).
40. M. Quante, S. P. Tu, H. Tomita, T. Gonda, S. S. W. Wang, S. Takashi, G. H. Baik, W. Shibata, B. DiPrete, K. S. Betz, R. Friedman, A. Varro, B. Tycko, T. C. Wang, Bone marrow-derived myofibroblasts contribute to the mesenchymal stem cell niche and promote tumor growth. *Cancer Cell* **19**, 257–272 (2011).
41. A. Mammoto, K. M. Connor, T. Mammoto, C. W. Yung, D. Huh, C. M. Aderman, G. Mostoslavsky, L. E. H. Smith, D. E. Ingber, A mechanosensitive transcriptional mechanism that controls angiaogenesis. *Nature* **457**, 1103–1108 (2009).
42. H. Nakagawa, S. Liyanarachchi, R. V. Davuluri, H. Auer, E. W. Martin, A. de la Chapelle, W. L. Frankel, Role of cancer-associated stromal fibroblasts in metastatic colon cancer to the liver and their expression profiles. *Oncogene* **23**, 7366–7377 (2004).
43. S. K. Gupta, M. Guo, Equilibrium and out-of-equilibrium mechanics of living mammalian cytoplasm. *J. Mech. Phys. Solids* **107**, 284–293 (2017).
44. Y. L. Han, P. Ronceray, G. Xu, A. Malandrino, R. D. Kamm, M. Lenz, C. P. Broedersz, M. Guo, Cell contraction induces long-ranged stress stiffening in the extracellular matrix. *Proc. Natl. Acad. Sci. U.S.A.* **115**, 4075–4080 (2018).
45. M. J. Paszek, N. Zahir, K. R. Johnson, J. N. Lakins, G. I. Rozenberg, A. Gefen, C. A. Reinhart-King, S. S. Margulies, M. Dembo, D. Boettiger, D. A. Hammer, V. M. Weaver, Tensional homeostasis and the malignant phenotype. *Cancer Cell* **8**, 241–254 (2005).
46. A. J. Merrell, B. Z. Stanger, Adult cell plasticity in vivo: de-differentiation and transdifferentiation are back in style. *Nat. Rev. Mol. Cell Biol.* **17**, 413–425 (2016).
47. P. W. Tetteh, O. Basak, H. F. Farin, K. Wiebrands, K. Kretzschmar, H. Begthel, M. van den Born, J. Korving, F. de Sauvage, J. H. van Es, A. van Oudenaarden, H. Clevers, Replacement of lost Lgr5-positive stem cells through plasticity of their enterocyte-lineage daughters. *Cell Stem Cell* **18**, 203–213 (2016).
48. B. Lin, J. H. Coleman, J. N. Peterson, M. J. Zunitch, W. Jang, D. B. Herrick, J. E. Schwob, Injury induces endogenous reprogramming and dedifferentiation of neuronal progenitors to multipotency. *Cell Stem Cell* **21**, 761–774.e5 (2017).
49. P. R. Tata, H. Mou, A. Pardo-Saganta, R. Zhao, M. Prabhu, B. M. Law, V. Vinarsky, J. L. Cho, S. Breton, A. Sahay, B. D. Medoff, J. Rajagopal, Dedifferentiation of committed epithelial cells into stem cells in vivo. *Nature* **503**, 218–223 (2013).
50. A. Elosegui-Artola, I. Andreu, A. E. M. Beedle, A. Lezamiz, M. Uroz, A. J. Kosmalska, R. Oria, J. Z. Kechagia, P. Rico-Lastres, A. L. le Roux, C. M. Shanahan, X. Trepat, D. Navajas, S. Garcia-Manyes, P. Roca-Cusachs, Force triggers YAP nuclear entry by regulating transport across nuclear pores. *Cell* **171**, 1397–1410.e14 (2017).
51. T. L. Downing, J. Soto, C. Morez, T. Houssin, A. Fritz, F. Yuan, J. Chu, S. Patel, D. V. Schaffer, S. Li, Biophysical regulation of epigenetic state and cell reprogramming. *Nat. Mater.* **12**, 1154–1162 (2013).
52. M. Caiazzo, Y. Okawa, A. Ranga, A. Piersigilli, Y. Tabata, M. P. Lutolf, Defined three-dimensional microenvironments boost induction of pluripotency. *Nat. Mater.* **15**, 344–352 (2016).
53. B. Roy, S. Venkatachalapathy, P. Ratna, Y. Wang, D. S. Jokhun, M. Nagarajan, G. V. Shivashankar, Laterally confined growth of cells induces nuclear reprogramming in the absence of exogenous biochemical factors. *Proc. Natl. Acad. Sci. U.S.A.* **115**, E4741–E4750 (2018).
54. http://www.brocku.ca/researchers/peter_rand/osmotic/osfile.html.
55. N. E. Wolins, B. K. Quaynor, J. R. Skinner, A. Tzekov, C. Park, K. Choi, P. E. Bickel, OP9 mouse stromal cells rapidly differentiate into adipocytes: Characterization of a useful new model of adipogenesis. *J. Lipid Res.* **47**, 450–460 (2006).
56. H. Mizuno, P. A. Zuk, M. Zhu, P. H. Lorenz, P. Benhaim, M. H. Hedrick, Myogenic differentiation by human processed lipoaspirate cells. *Plast. Reconstr. Surg.* **109**, 199–209 (2002).
57. P. A. Zuk, M. Zhu, P. Ashjian, D. A. de Ugarte, J. I. Huang, H. Mizuno, Z. C. Alfonso, J. K. Fraser, P. Benhaim, M. H. Hedrick, Human adipose tissue is a source of multipotent stem cells. *Mol. Biol. Cell* **13**, 4279–4295 (2002).
58. P. A. Zuk, M. Zhu, H. Mizuno, J. Huang, J. W. Futrell, A. J. Katz, P. Benhaim, H. P. Lorenz, M. H. Hedrick, Multilineage cells from human adipose tissue: Implications for cell-based therapies. *Tissue Eng.* **7**, 211–228 (2001).
59. O. Juffroy, D. Noël, A. Delanoye, O. Viltart, I. Wolowczuk, C. Verwaerde, Subcutaneous graft of D1 mouse mesenchymal stem cells leads to the formation of a bone-like structure. *Differentiation* **78**, 223–231 (2009).
60. J. Guerrero, N. Tobar, M. Cáceres, L. Espinoza, P. Escobar, J. Dotor, P. C. Smith, J. Martínez, Soluble factors derived from tumor mammary cell lines induce a stromal mammary adipose reversion in human and mice adipose cells. Possible role of TGF-β1 and TNF-α. *Breast Cancer Res. Treat.* **119**, 497–508 (2010).
61. P. Bi, F. Yue, A. Karki, B. Castro, S. E. Wirbisky, C. Wang, A. Durkes, B. D. Elzey, O. M. Andrisani, C. A. Bidwell, J. L. Freeman, S. F. Konieczny, S. Kuang, Notch activation drives adipocyte dedifferentiation and tumorigenic transformation in mice. *J. Exp. Med.* **213**, 2019–2037 (2016).
62. M. Suzuki, Y. Shinohara, Y. Ohsaki, T. Fujimoto, Lipid droplets: Size matters. *J. Electron Microsc.* **60**, S101 (2011).
63. F. Wilfling, J. T. Haas, T. C. Walther, R. V. Farese Jr., Lipid droplet biogenesis. *Curr. Opin. Cell Biol.* **29**, 39–45 (2014).
64. H. Yang, A. Galea, V. Sytnyk, M. Crossley, Controlling the size of lipid droplets: Lipid and protein factors. *Curr. Opin. Cell Biol.* **24**, 509–516 (2012).
65. Y.-L. Wang, R. J. Pelham Jr., Preparation of a Flexible, Porous Polyacrylamide Substrate for Mechanical Studies of Cultured Cells. in *Methods in Enzymology* (Elsevier, 1998), vol. 298, pp. 489–496.
66. S. Wu, J. Chen, P. Dong, S. Zhang, Y. He, L. Sun, J. Zhu, Y. Cheng, X. Li, A. Tang, Y. Huang, Y. Gui, C. Liu, G. Yang, F. Zhou, Z. Cai, R. Wang, Global gene expression profiling identifies ALDH2, CCNE1 and SMAD3 as potential prognostic markers in upper tract urothelial carcinoma. *BMC Cancer* **14**, 836 (2014).
67. Y. Xie, G. Wu, J. Tang, R. Luo, J. Patterson, S. Liu, W. Huang, G. He, S. Gu, S. Li, X. Zhou, T. W. Lam, Y. Li, X. Xu, G. K. S. Wong, J. Wang, SOAPdenovo-Trans: De novo transcriptome assembly with short RNA-Seq reads. *Bioinformatics* **30**, 1660–1666 (2014).
68. S. Audic, J. M. Claverie, The significance of digital expression profiles. *Genome Res.* **7**, 986–995 (1997).

69. A. Dabney, J. D. Storey, G. Warnes, qvalue: Q-value estimation for false discovery rate control. *R package version* **1**, (2010).
70. E. H. Zhou, X. Trepat, C. Y. Park, G. Lenormand, M. N. Oliver, S. M. Mijailovich, C. Hardin, D. A. Weitz, J. P. Butler, J. J. Fredberg, Universal behavior of the osmotically compressed cell and its analogy to the colloidal glass transition. *Proc. Natl. Acad. Sci. U.S.A.* **106**, 10632–10637 (2009).

Acknowledgments
Funding: We acknowledge the support from the National Cancer Institute (grant 1U01CA202123) and the MIT Jeptha H. and Emily V. Wade Award. A.S.M., B.R.S., T.-Y.S., and D.J.M. are supported by the NIH 5R01 DE013033 and 2R01 DE013349. **Author contributions:** M.G., A.S.M., and Y.L. designed the research. M.G. led the project. Y.L., M.G., S.K.G., and D.J.M. wrote the manuscript. Y.L. conducted most of the experiments. A.S.M., M.C., and Y.L.H. contributed cell lines, new reagents, and analytical tools. A.S.M., B.R.S., and T.-Y.S. carried out the xenograft mouse experiments. X.Z. performed the RNA-seq experiments. Y.L., A.S.M., B.R.S., and X.Z. analyzed the data. **Competing interests:** The authors declare that they have no competing interests. **Data and materials availability:** All primary data are included in the source data associated with each figure accompanying this paper. The sequences reported in this paper have been deposited in the NCBI Short Read Archive (accession no. PRJNA554910). Additional data related to this paper may be requested from the authors.

Submitted 3 April 2019
Accepted 25 November 2019
Published 22 January 2020
10.1126/sciadv.aax5611

Citation: Y. Li, A. S. Mao, B. R. Seo, X. Zhao, S. K. Gupta, M. Chen, Y. L. Han, T.-Y. Shih, D. J. Mooney, M. Guo, Compression-induced dedifferentiation of adipocytes promotes tumor progression. *Sci. Adv.* **6**, eaax5611 (2020).

Science Advances

Compression-induced dedifferentiation of adipocytes promotes tumor progression

Yiwei Li, Angelo S. Mao, Bo Ri Seo, Xing Zhao, Satish Kumar Gupta, Maorong Chen, Yu Long Han, Ting-Yu Shih, David J. Mooney and Ming Guo

Sci Adv **6** (4), eaax5611.
DOI: 10.1126/sciadv.aax5611